Engineering Solid Mechanics 11 (2023) 311-324

Contents lists available at GrowingScience

Engineering Solid Mechanics

homepage: www.GrowingScience.com/esm

Hot workability characteristics of two A335 P92 steels for power plant application: A comparative study

J.O. Obiko[a,b*], L.H. Chown[a,c], D.J. Whitefield[c] and M.O. Bodunrin[a,c]

[a]*School of Chemical and Metallurgical Engineering, University of the Witwatersrand, 1 Jan Smuts Avenue, Johannesburg, 2000, South Africa*
[b]*Department of Mining, Materials and Petroleum Engineering, Jomo Kenyatta University of Agriculture and Technology Nairobi, Kenya*
[c]*DSI-NRF Centre of Excellence in Strong Materials, hosted by the University of the Witwatersrand, South Africa*

ARTICLE INFO

Article history:
Received 16 August 2022
Accepted 2 February 2023
Available online
2 February 2023

Keywords:
Metal workability
Flow stress
Constitutive equation
Metal forming
P92 steel

ABSTRACT

The article reports on the workability of two P92 steels having a chromium content of 8.29 and 9.48 wt%. Constitutive equations were used to calculate material parameters describing the hot deformation flow stress. Hot deformation tests were conducted using the Gleeble® 3500 thermomechanical facility. Test conditions were: temperature of 850-1000°C and strain rate of 0.1-10s^{-1} to a strain of 0.5. The flow stress curve results show that dynamic recovery was the only softening mechanism. A comparative study of the two steels revealed that Cr content had a marginal significance on the flow stress behaviour. Constitutive analysis results of the material parameters were: a stress exponent of 9.0 (P92-A), and 11.0 (P92-B), while the activation energy was 369 $kJmol^{-1}$ (P92-A), and 472 $kJmol^{-1}$ (P92-B). A brief explanation of the material parameter results is in this article. A flow stress model was developed to predict the flow stress behaviour of the two P92 steels investigated. The results show that the model accurately predicts the flow stress at all the deformation conditions applied. The statistical parameters showed a good correlation between the predicted and the experimental data. Therefore, this model can be used to develop metal forming schedules for industrial applications.

1. Introduction

The study of metal forming such as forging and rolling plays an important role in understanding the shaping process and microstructure evolution of the finished components (Lin et al., 2009). Thorough understanding of metal flow patterns and phase transformation during forming provides a better description of metal flow properties (Lin et al., 2008). Hence, providing information on the design of these forming processes. Constitutive equations usually describe the effects of deformation condition flow stress. These equations act as an input into a computer program code for macroscale simulation of the metal forming process (Lin et al., 2008, 2009; Yan et al., 2013). The constitutive models for predicting flow stress fall under three models: empirical, neural networks and physical models (He et al., 2015). These models have their advantages and disadvantages. However, the models are used to describe forming behaviour of metal during forming. Studies have used empirical models (e.g. Arrhenius-type equation) widely to study how deformation conditions affect flow stress (He et al., 2013, 2015; Liu et al., 2013; Mirzadeh, 2015; Mirzadeh et al., 2011; Qian et al., 2015). Several researchers have used the Arrhenius type model to characterise the flow stress behaviour of a variety of materials such as modified 9Cr-1Mo steel (Samantaray et al., 2010), P92 steel (Alsagabi, 2016; Liu et al., 2011; Obiko et al., 2019; Sun et al., 2010), 35CrMo steel (Huang et al., 2017), 20CrMo alloy steel (He et al., 2013), Nickel-based superalloy (Zhang et al., 2016), N08028 corrosion-resistant alloy (Wang et al., 2013), aluminium alloys (Lin et al., 2010; Mostafaei & Kazeminezhad, 2012) and magnesium alloys (Luan et al., 2014) and titanium alloys (Jha et al., 2017). The flow stress behaviour is predicted by fitting experimental data into the constitutive equations to determine material constants. These constitutive equations act as input codes for modelling metal forming (Lin et al., 2010).

* Corresponding author.
E-mail addresses: japheth.obiko97@gmail.com (J.O. Obiko)

ISSN 2291-8752 (Online) - ISSN 2291-8744 (Print)

doi: 10.5267/j.esm.2023.2.001

P92 steel has become popular in manufacturing power plant components, which operate at high temperatures and pressure. These conditions result in higher efficiency and reduced carbon dioxide (CO_2) emissions (David et al., 2013). For the structural plant components to withstand the working conditions, the structural materials should have high strength and creep resistance (Ohgami et al., 1997). The development of ferritic steels that can withstand power plant conditions has received attention. Concerted studies have resulted in the development of P92 steel (Francis et al., 2006). P92 steel is a variant of P91 steel by adding 1.8-2.0 wt% tungsten and 0.5 molybdenum (Výrostková et al., 2008). This steel has wide application in modern ultra-supercritical power plant structural components (Tabuchi et al., 2001).

This steel exhibit superior properties such as corrosion resistance, high strength, high creep resistance and ease of fabrication for long term power plant applications (Alsagabi, 2016; Liu et al., 2011; Shi & Liu, 2011). Compared to the other 9-12%Cr steels such as P91, E911 and P122 (Czyrska-filemonowicz et al., 2006), P92 steels exhibit long creep life and a higher strength-to-weight ratio for the production of boiler pipes and turbines sections. P92 steel has high strength of about 30% higher than P91 steel for prolonged power plant in-service applications (Ohgami et al., 1997). Hence, it has become a promising material for the new generation ultra-supercritical power plant structural components. The reason is that P92 can operate at higher temperatures (up to 650°C) compared to earlier steels such as P91 steel (593°C) (Ennis & Czyrska-Filemonowicz, 2003). Tungsten and molybdenum elements in P92 steel improve the creep resistance enhancing the solid solution strengthening (Czyrska-filemonowicz et al., 2006). Ohgami *et al.*(1997) showed that the allowable stress of P92 steel is 1.3 times that of P91 steel during service at 600 °C. Also, a pipe wall thickness of only 98.4 mm, is needed for P92 steel compared to 141.2 mm for P91 steel operating at 610 °C and 27.5 MPa. These additions reduced the production cost of P92 pipes. The reduction in wall thickness reduces thermal stress during shut down and start-up of the boiler, thus improving the structural integrity during long-term creep conditions.

Creep properties of P92 steel have been reported widely in the literature (Sakthivel et al., 2016; Samuel et al., 2013; Yatomi et al., 2010). There is scarce data in the literature about forming behaviour of this steel during production. This information is vital should the need to reuse the steel arise after it is exhausted by creep under service conditions. The study of the flow behaviour of P92 steel as affected by alloying elements is also missing in the literature. Alloying elements play a role in the microstructure evolution during deformation. Hence, the elemental content on the flow pattern can be analysed using the constitutive equations that describe the flow stress of a given material (Wahabi et al., 2003).

The study investigated the hot deformation behaviour of two A335 P92 steels having different chromium content. The variation in Cr content was within the steel composition standard specification. Chromium is the prime alloying element in P92 ferritic-martensitic steel at 8-9 wt% Cr and enhances creep strength by precipitation of Cr-rich $M_{23}C_6$ carbides during tempering. These carbides result in the solution strengthening the microstructure by increasing the pinning dislocation motion (Czyrska-filemonowicz et al., 2006). A high Cr (up to 20 wt%) content improves the corrosion resistance under service conditions (Masuyama, 2001). The 9 wt% Cr content in P92 steel is insufficient to provide oxidation resistance at 650°C in power plants, as reported by Masuyama (2001). More than 13% Cr results in delta-ferrite formation, which harms the mechanical properties of steel (Masuyama, 2001). The structural integrity of components parts such as header, boiler pipes and tubes depends on the production process parameters, which affect microstructure evolution and hence, the mechanical properties (Samantaray et al., 2010). The mechanical properties, especially the deformation behaviour of metals and alloys, are best studied using flow stress curves. These curves provide information on deformation mechanisms occurring during forming, whether cold, warm or hot. For example, creep resistance steel will exhibit flow stress curves showing a dynamic softening (DRV or DRX) during forming. These curves show an increase in flow stress to the peak stress and then reach or fall to a steady-state condition. The flow curves show the microstructure evolution occurring during forming. Hence, analyses of the flow behaviour are necessary for defining the workability of metals and alloys. The flow behaviour of the two A335 P92 steels was analysed using Arrhenius equations. The equations for describing the metal flow pattern for the two A335 P92 steels were derived. A comparative analysis of the constitutive parameters and the effect of Cr on flow stress behaviour for the two steels is explained in detail. The validity of the developed models was also investigated and reported in this paper.

2. Experimental procedure

P92 steel samples of 8 mm diameter and 12 mm length were machined for uniaxial compression in the Gleeble® 3500 machine. The test samples were machined parallel to the direction of forging of as-received test samples. The chemical composition for the two steels used for the tests is as shown in **Table 1**. The chromel-alumel K-type thermocouples were welded midspan to measure test temperature and monitor the preset temperature during testing. The specimen and the anvil ends were sprayed with nickel paste and graphite foil in between them to reduce friction. Test temperatures were: 850, 900, 950 and 1000°C, and strain rates of 0.1, 1 and 10 s^{-1}. These temperatures are typical for forging in the single-phase austenite range of P92 steel for good workability (Kishor et al., 2016). The deformation schedule is given systematically in **Fig. 1**. The specimen samples were deformed to a true strain of 0.5. Austenitisation temperature of 1100 °C was chosen, as it is above the dissolution temperature of $M_{23}C_6$ carbide (Kumar et al., 2017). At this temperature (1100 °C), these carbides will dissolve during the austenitisation stage.

Table 1. Chemical composition of the two P92 tested steels

Sample	C	Mn	Si	Cr	Mo	Ni	Cu	Al	V	Nb	W	Co
P92-A	0.10	0.39	0.20	8.29	0.65	0.19	0.08	0.012	0.16	0.093	2.07	0.015
P92-B	0.11	0.32	0.25	9.48	0.61	0.17	-	0.023	0.20	0.076	2.34	0.024

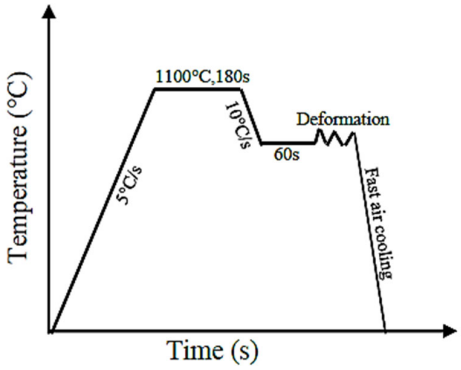

Fig. 1. Uniaxial compression test profile

3. Results and Discussion

This study did not consider the effect of temperature rise due to adiabatic heating during forming since the procedure, as detailed by Samantaray *et al.* (2011), for measuring adiabatic heating during compression tests was not followed. However, the difference between the pre-set temperature and measured surface temperature in all deformation conditions was approximately below 20°C. This temperature variation did not cause variation in terms of flow stress. The uniaxial compression test data of flow stress-strain curves deviate from the actual values due to interfacial friction between the workpiece and dies. Therefore, to determine the actual values, many researchers have used analytical equations to eliminate the effect of interfacial friction from the flow stress curves. For more details on these equations, readers can refer to articles available in the literature to avoid repetition (Evans & Scharning, 2001; Wan et al., 2018). The flow stress values reported in this study were friction corrected.

3.1 Effect of deformation conditions on flow behaviour

Fig. 2 (P92-A)Fig**. 3** (P92-B) show the flow stress-strain curve of the two steels obtained during hot deformation. The flow stress curves show the material response to the deformation conditions (Wang et al., 2014). Generally, the two steels investigated exhibited a similar flow stress behaviour: the flow stress increased rapidly as the strain increased until steady-state flow stress, referred to as saturation flow stress (Laasraoui & Jonas, 1991). At strain 0.3 and below, the flow stress increased rapidly, showing a work hardening stage. With an increase in deformation, the flow stress attained a steady-state condition caused by dynamic softening (work hardening + DRV) (Laasraoui & Jonas, 1991). For the two steels, the flow stress−strain curves exhibited work hardening at strains < 0.3, followed by dynamic recovery as the softening mechanism at a higher deformation (greater than 0.3).

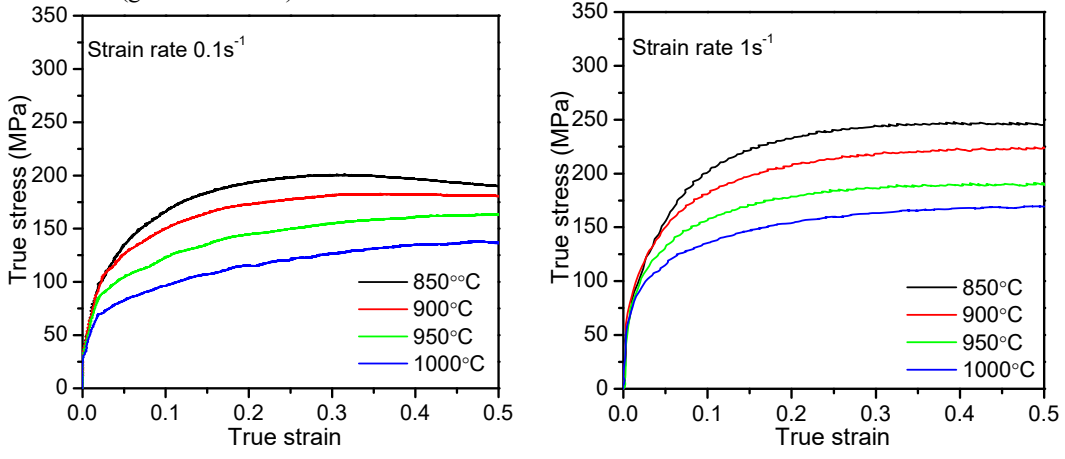

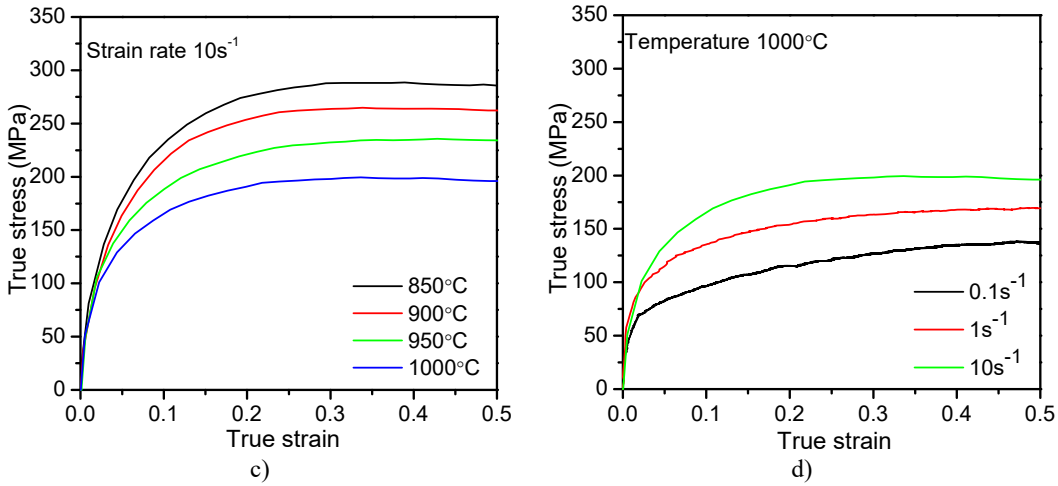

Fig. 2. Flow stress-strain curves for P92-A

The stress-strain curves show that the flow stress depends on the loading conditions. The variation in flow stress behaviour at different deformation conditions depends on the atom diffusion and dislocation movement, which is affected by deformation conditions (Zhu et al., 2018). The flow stress increased as the strain rate increased at a constant temperature. Generally, higher deformation temperature and lower strain rate result in lower flow stress. Flow stress decreases due to dynamic softening, especially DRV for P92 steel, availability of atomic vacancies, and dislocation diffusion. Higher deformation temperatures cause carbide dissolution, thus reducing precipitation hardening. In the absence of carbides, enhanced dislocation mobility occurs, lowering flow stress (Carsí et al., 2011). These conditions: higher temperature and lower strain rate, are favourable for metalworking.

At low deformation temperature and higher strain rate, higher flow stresses are experienced due to increased dislocation density, as deformation is too rapid for softening to occur. For example, the flow stress for P92-A steel increased by 44.7 % with an increase in strain rate from 0.1-10s^{-1} at 850°C as shown in **Fig. 2d**. Under similar conditions, the flow stress of P92-B by 32.8% **Fig. 3d.** However, at the highest deformation temperature of 1000°C and strain rate increase of 0.1 to 10 s^{-1}, the flow stress increase was much higher: 44.7% (P92-A) and 47.4% (P92-B). This result shows that the flow stress behaviour is very sensitive to the deformation conditions.

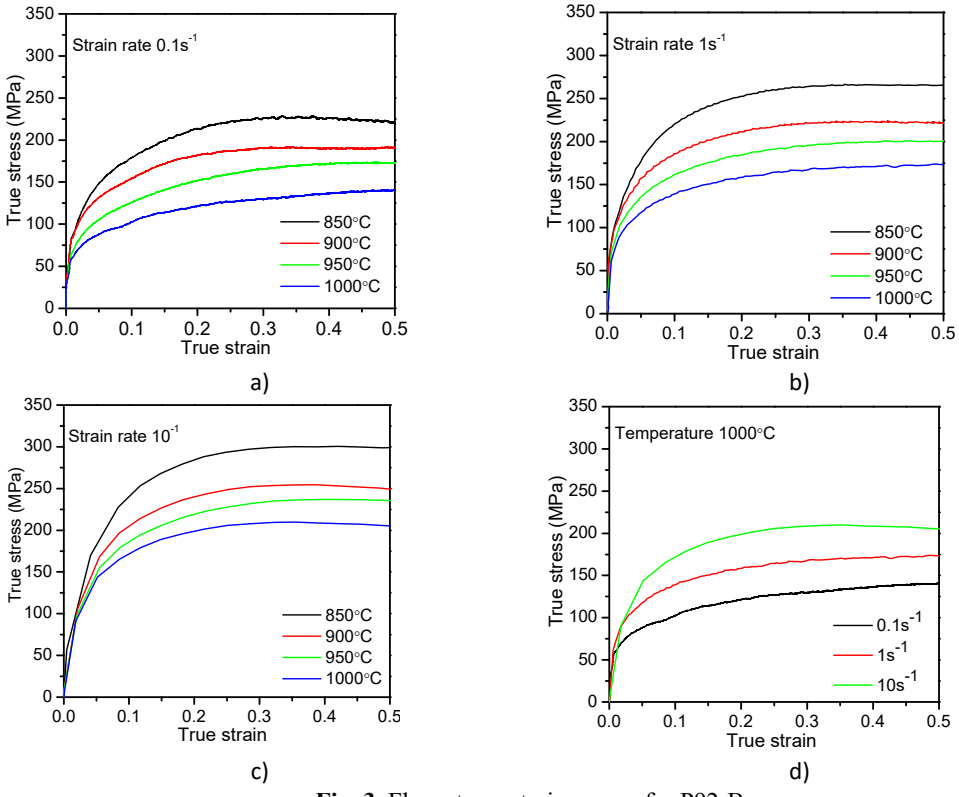

Fig. 3. Flow stress-strain curves for P92-B

Fig. 4 shows flow stress **vs**. temperature confirming that metal flow behaviour is sensitive to deformation conditions as mentioned earlier. The flow stress results indicate clearly that dynamic softening occurs at higher temperature deformation resulting in lower flow stress. A dynamic softening mechanism is a thermally activated process. This process accelerates at high deformation temperature. During metal forming, grain refinement occurs, resulting in improving material strength. An increase in the forming temperature may cause an increase in the average grain size at a given strain rate. Higher forming temperatures may cause the grain to grow, resulting in the formation of fine-equiaxed grains along the grain boundaries. These changes in the microstructure suggest that DRX partially occurred (Li et al., 2019). Lower deformation temperatures cause large plastic deformation force and stress resulting in uniform grain refinement (Yanushkevich et al., 2016). This condition ensures uniform fine-grain distribution across the deformed sample, thus improving mechanical properties such as creep strength. However, the temperature at which this behaviour occurs has to be determined.

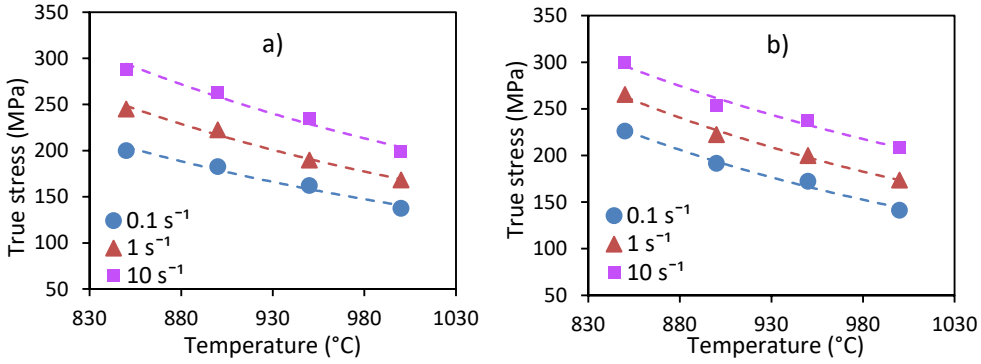

Fig. 4. Relationship between maximum flow stress, strain rate and temperature for hot deformation a) P92-A, and b) P92-B steel

Forming conditions such as lower deformation temperature and high strain rate, defects may occur, resulting in poor mechanical properties. Flow deformation defects likely to occur at lower deformation temperatures include: wedging cracking, shear bands, and flow localisation. These defects are detrimental to the mechanical performance of the final product (Lin et al., 2013). For the production of high-quality products, optimisation of deformation temperature is paramount. Microstructure evolution during forming is directly affected by the deformation conditions. The mechanical properties of the final product depend on its microstructure. Therefore, forming parameters such as deformation temperature for industrial processes needs to be optimised.

The stress values for the two steels investigated show a minor difference under all tested conditions. **Table 2** summarises the measured stress values from the study. The results show that P92-B had the highest stress values for the conditions tested. These high flow stress values result from higher solute content in P92-B steel, especially chromium. The chromium content enhances carbide formation, which causes solution strengthening, hindering dislocation. (Czyrska-filemonowicz et al., 2006). Chromium contributes to the formation of $M_{23}C_6$ carbides. The presence of $M_{23}C_6$ carbides may cause variation in the flow stress. Carsí *et al.* (2011) reported that a small amount of $M_{23}C_6$ carbides hinders dislocation motion, increasing the stress exponent, hence higher flow stress. Forging below upper transformation temperature (Ae3), higher deformation resistance is expected since the martensite phase is stronger than the austenite phase, resulting in higher flow stress. Therefore, forging at austenitic field temperatures is advised. The absence of carbides in the austenite field makes the material less resistant to deformation (Carsí et al., 2011). In the current study, the selected deformation temperatures were above Ae3, hence occurred at the austenite field. $M_{23}C_6$ carbides had dissolved at these deformation temperatures resulting in higher ductility in the austenitic phase field. Lower flow stresses were obtained at a deformation temperature of 1000°C compared to 850-950°C for the two steels.

The flow stress-strain curves (**Fig. 2-Fig. 3**) indicate that the flow stress is strongly strain rate sensitive. Zhu, He and Zhang (2018) reported that at a higher deformation rate, deformation occurs quickly and there is limited time for the dislocation and rearrangement to counteract, resulting in higher flow stress. Contrary, at a lower deformation rate, deformation is slow enabling dislocation motion to occur, hence lower flow stress. The impact of strain rate on flow stress behaviour can be due to the deformation mechanisms which control the metal flow pattern (Rastegari et al., 2015).

3.2 Constitutive modelling analysis

According to Sellars and McTegart (1966), the flow stress behaviour can be characterised using Eq. (1) over a wide range of flow stresses:

$$\dot{\varepsilon} = A\,[sinh\,(\alpha\sigma)]^n\,exp\left(\frac{-Q}{RT}\right) \tag{1}$$

In Eq. (1), *A, α, and n σ* and *Q* are material constants. The material constants are calculated using peak or steady-state stress in the constitutive equation (McQueen & Ryan, 2002). In this study, the flow stress-strain curves, as shown in **Figs. 2-3**, did not exhibit distinct characteristic points such as peak or steady-state stress. Alternatively, the saturation flow stress obtained from the flow stress-strain curves assists in analysing flow behaviour using the constitutive equation (Laasraoui & Jonas, 1991; Oudin, Barnett and Hodgson, 2004). Therefore, the hyperbolic sine-law equation is:

$$Z = \dot{\varepsilon} exp\left(\frac{Q}{RT}\right) = A\ [sinh\ (\alpha\sigma_{sat})]^n \tag{2}$$

To avoid repetition, the constitutive equations for determining material constants is summarised herein.

$$n' = \frac{\partial ln\dot{\varepsilon}}{\partial ln\sigma_{sat}} \text{ (low flow stress)} \tag{3}$$

$$\beta = \frac{\partial ln\dot{\varepsilon}}{\partial \sigma_{sat}} \text{ (higher flow stress)} \tag{4}$$

$$\text{and} \quad \alpha = \beta/n' \tag{5}$$

Under constant temperature:

$$\frac{1}{n} = \frac{\partial ln[sinh\ (\alpha\sigma_{sat})]}{\partial ln\dot{\varepsilon}} \tag{6}$$

Under constant strain rate $\dot{\boldsymbol{\varepsilon}}$**:**

$$Q = Rn\frac{\partial ln[sinh\ (\alpha\sigma_{sat})]}{\partial \frac{1}{T}} \tag{7}$$

The constitutive constants: *α, β, n', n and Q* in Eqs. (3-7) were obtained using the linear regression method for the two steels investigated. The calculated values are as tabulated in **Table 3**. The linear regression models built to calculate *α, β, n', n and Q* for the two steels are, as shown in **Figs. 5-8**. The Q-values for the two steels at a strain of 0.5 were: P92-A (369 kJmol^{-1}) and P92-B (472 kJmol^{-1}). These Q-values are within range from those reported in literature of 437 kJ.mol^{-1} (Shi & Liu, 2011), 498.9 kJ.mol^{-1} (Liu et al., 2011), 390 kJ.mol^{-1} (Carsí et al., 2011), and 565 kJ.mol^{-1} (Sun et al., 2010). However, the *Q* values obtained were higher than those for self-diffusion *γ*-Fe in austenite of 270 kJ.mol^{-1} (Cabrera et al., 1997). The *Q* value indicates the material resistance to deformation (Yang et al., 2015). Table The Q-values variation for P92 steel can be due to alloying elements, especially chromium. The chromium content increases the stacking fault energy of the steel. A higher stacking fault energy affects the dissociation of dislocations, thus affecting the ability of dislocation cross-slip (Medina & Hernandez, 1996; Nkhoma, 2014).

Table 2. The flow stress data for the two P92 steels.

Steel	$\dot{\boldsymbol{\varepsilon}}$ (s^{-1})	850°C	900°C	950°C	1000°C
P92-A	0.1	199.91	182.53	162.07	137.49
	1	245.04	222.48	189.73	168.22
	10	288.06	263.48	234.77	198.95
P92-B	0.1	226.06	191.45	172.29	141.25
	1	265.50	222.48	199.84	173.51
	10	300.22	253.61	236.82	208.14

The stress data from this study for the two steels (Table 2) had different stress values at the same deformation conditions. P92-B had the highest value of flow stress in all the deformation conditions causing high activation energy. Higher Cr content in this steel (P92-B) than in P92-A steel caused higher activation energy. Funakawa and Ujiro (2010) reported that a 1.0 mass% Cr addition causes an increase of yield stress by 5.6 MPa in low carbon steel. The strength increases due to the effect of Cr in solution strengthening, which directly influences the activation energy. The actual contribution of Cr on metal forming behaviour has attracted mixed reactions from different researchers. Mehtonen, Karjalainen and Porter (2014) reported that higher Cr content results in dynamic softening causing low activation energy *Q* during deformation. However, they investigated stainless steel, which is quite different from the steel studied currently, even though the deformation conditions were relatively the same. A study by Zhu *et al.* (2021), reported that higher Cr content causes the formation of chromium carbide $Cr_{23}C_6$ of chromium nitride (CrN), which affects the material toughness. Carbides or nitrides formation causes a softening effect due to the removal of N and C from the matrix resulting in a reduction in solid solution hardening. However, this is not the case in the present study because higher Cr content caused an increase in flow stress and apparent activation energy. There is a need for further study to establish the role of Cr in softening of steels during deformation. To this end, Cr content in steel influences the flow behaviour, thus affecting activation energy. *Q*-value is a function of alloying elements. Activation energy increases with an increase of alloying elements (Yang et al., 2017). Therefore, the differences in the activation energy (Table 3) of the steels investigated can be due to their differences in Cr content. An increase in Cr content

(P92-B) results in either solid solution strengthening or precipitation hardening by controlling the formation of carbides pinning dislocation at the grain boundary. Both solid-solution and precipitation strengthening processes may affect the workability of a material.

Table 3. Material constants calculated using the constutive equations.

Steel	n	Q	ln A	n′	β′	α
P92-A	9	369	35.43	12.46	0.062	0.0049
P92-B	11	472	45.68	14.70	0.069	0.0047

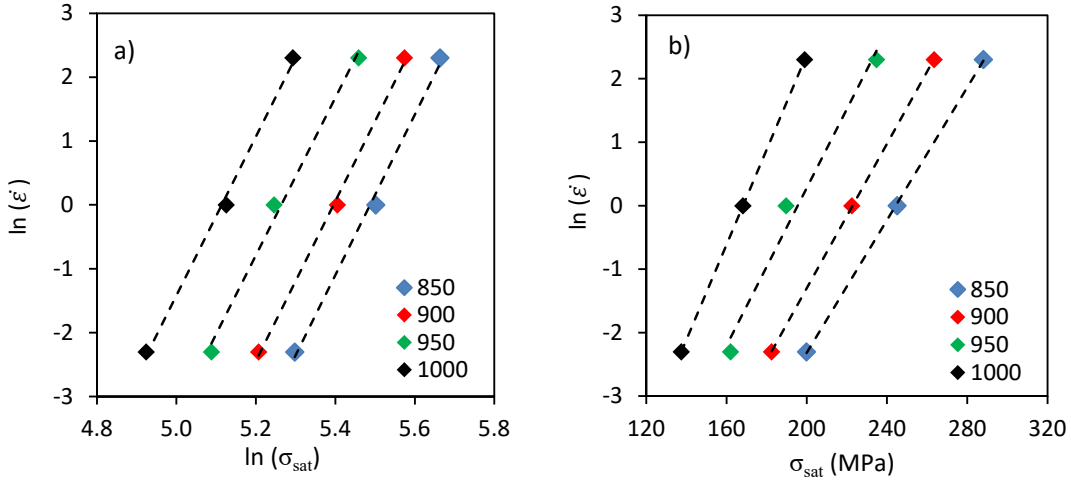

Fig. 5. P92-A: a) Plot of ln ($\dot{\varepsilon}$) *vs.* ln σ_{sat} gives n', and b) ln ($\dot{\varepsilon}$) *vs.* σ_{sat} gives β.

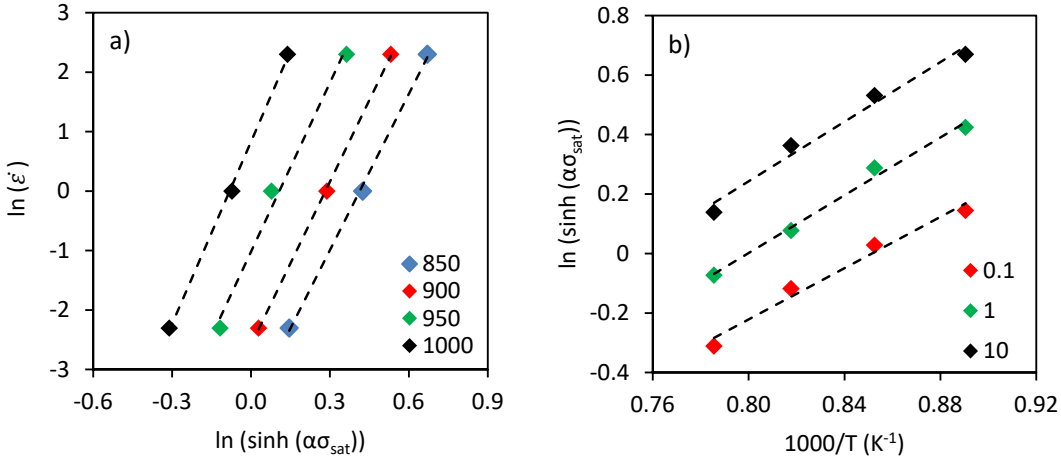

Fig. 6. P92-A: a) Plot of ln ($\dot{\boldsymbol{\varepsilon}}$) *vs.* ln (sinh ($\alpha\sigma_{sat}$) gives n, and b) ln (sinh ($\alpha\sigma_{sat}$)) *vs.* 1000/T gives Q

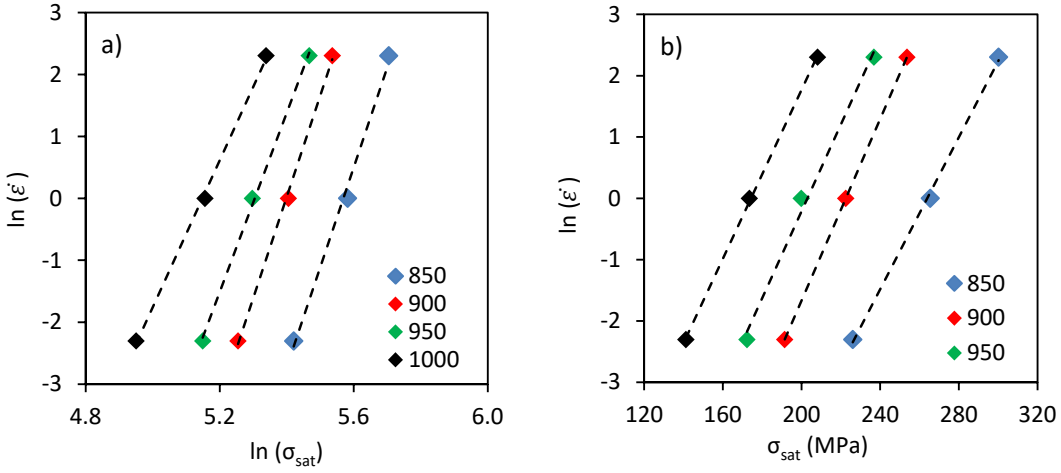

Fig. 7. P92-A: a) Plot of ln ($\dot{\boldsymbol{\varepsilon}}$) *vs.* ln σ_{sat} gives n', and b) ln ($\dot{\boldsymbol{\varepsilon}}$) *vs.* σ_{sat} gives β

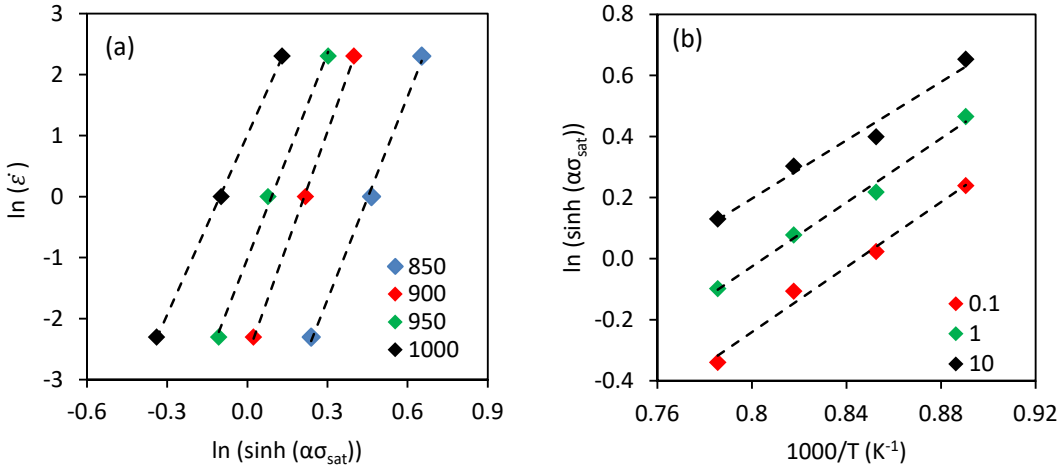

Fig. 8. P92-B: a) Plot of ln ($\dot{\varepsilon}$) *vs.* ln(sinh ($\alpha\,\sigma_{sat}$)) gives *n,* and b) ln(sinh ($\alpha\,\sigma_{sat}$)) *vs.* 1000/*T* gives Q

From the above analysis, the flow stress of the two steels studied can be described by:

P92-A: $$\dot{\varepsilon} = 2.44 \times 10^{15} \sinh(0.0049\sigma_{sat})^{9} \exp\left[\frac{-369000}{RT}\right] \quad (8)$$

P92-B: $$\dot{\varepsilon} = 6.90 \times 10^{19} \sinh(0.0045\sigma_{sat})^{11} \exp\left[\frac{-471860}{RT}\right] \quad (9)$$

Further solving Eq. (1) derives the following Zener-Hollomon equation:

$$\sigma_{sat} = \frac{1}{\alpha}\ln\left\{\left(\frac{Z}{A}\right)^{1/n} + \left[\left(\frac{Z}{A}\right)^{2/n} + 1\right]^{1/2}\right\} \quad (10)$$

Using Eq. (10), the flow stress can be determined using the Zener-Hollomon equation. The equation for the two steels can be written as:

P92-A: $$\sigma_{sat} = \frac{1}{0.0049}\ln\left[\left(\frac{Z}{2.44\times10^{15}}\right)^{\frac{1}{9}} + \left(\left(\frac{Z}{2.44\times10^{15}}\right)^{\frac{2}{9}} + 1\right)^{\frac{1}{2}}\right] \quad (11)$$

$$Z = \dot{\varepsilon} exp\left[\frac{369000}{RT}\right] = 2.44 \times 10^{15}(\sinh(0.0049\sigma_{sat})^{9}$$

P92-B: $$\sigma_{sat} = \frac{1}{0.0045}\ln\left[\left(\frac{Z}{6.90\times10^{19}}\right)^{\frac{1}{11}} + \left(\left(\frac{Z}{6.90\times10^{19}}\right)^{\frac{2}{11}} + 1\right)^{\frac{1}{2}}\right] \quad (12)$$

$$Z = \dot{\varepsilon} exp\left[\frac{472000}{RT}\right] = 6.90 \times 10^{19}\,(\sinh(0.0045\sigma_{sat})^{11}$$

The effect of deformation temperature and the strain rate can be represented by the Zener Hollomon parameter **Z** as given in Eq. (2). Eq. (2) gives the relationship between ln **Z** and ln (sinh (**ασsat**)), as shown in **Fig. 9**. The intercept of the linear regression line gives the value of ln **A**. The parameter A and linear correlation coefficient values are in **Table 4.**

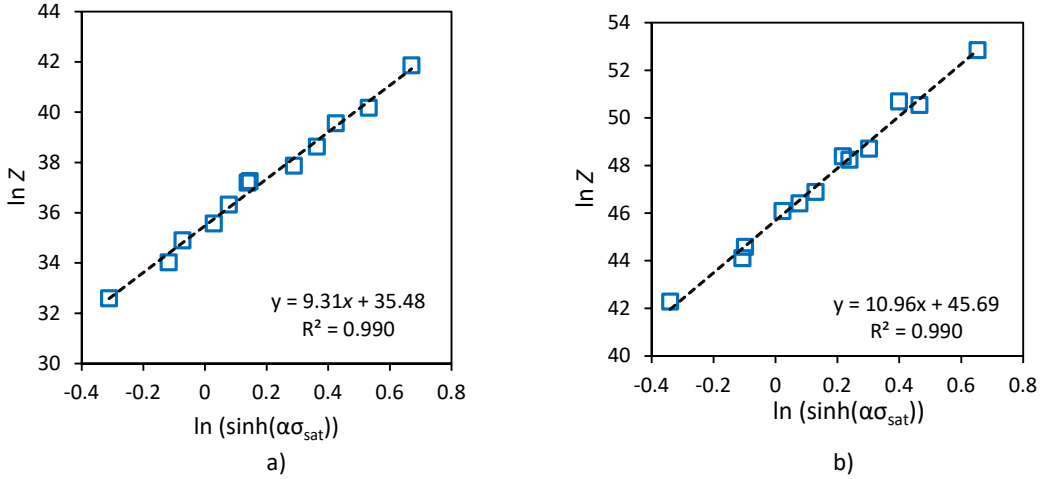

Fig. 9. Plot of ln *Z vs.*ln (sinh ($\alpha\sigma_{sat}$)) a) P92-A, and b) P92-B

Table 4. Calculated material constant *A* and linear correlation coefficient R^2

Steel	ln A	R^2	A
P92-A	35.43	0.99	2.56×10^{15}
P92-B	45.68	0.99	6.94×10^{19}

3.3 Effect of composition on constitutive parameters and flow stress prediction

Fig. 10 is an SEM micrograph of the two-steel studied exhibiting distinct grain and lath boundaries and martensite microstructure. The bright carbides are seen along the prior grain austenite and lath boundaries. The visible precipitates using a scanning electron microscope are mainly $M_{23}C_6$ (M = Fe, Mo, W, Cr) carbides (Czyrska-filemonowicz et al., 2006; Sakthivel et al., 2015). These precipitates enhance strengthening by pinning dislocation motion during forming, thus improving mechanical properties (Milović et al., 2013). The SEM images in **Fig. 10** show that the carbides precipitated at the grain boundary, and the strengthening effect should be similar. Then, their contribution to resistance during deformation may be of equal strength. The constitutive analysis shows that the differences in the deformation constant were significant in stress exponent values (9.0 for P92-A and 11.0 for P92-B), and the structure factor of P92-B was two-order of magnitude than P92-A, while the activation energies were: 369 $kJmol^{-1}$ (P92-A), and 472 $kJmol^{-1}$ (P92-B). These constants indicate a slight difference in the flow behaviour of the two steels. However, further analysis in using either of the developed constitutive models of the two steels to predict flow stress behaviour gave no difference in flow stress value, as shown in **Fig. 11**. Then, the question is, what is causing the differences in their flow stress values? Could the difference emanate from the contribution of other minor alloying elements? The conclusion can be that minor alloying elements caused the differences since deformation conditions were the same.

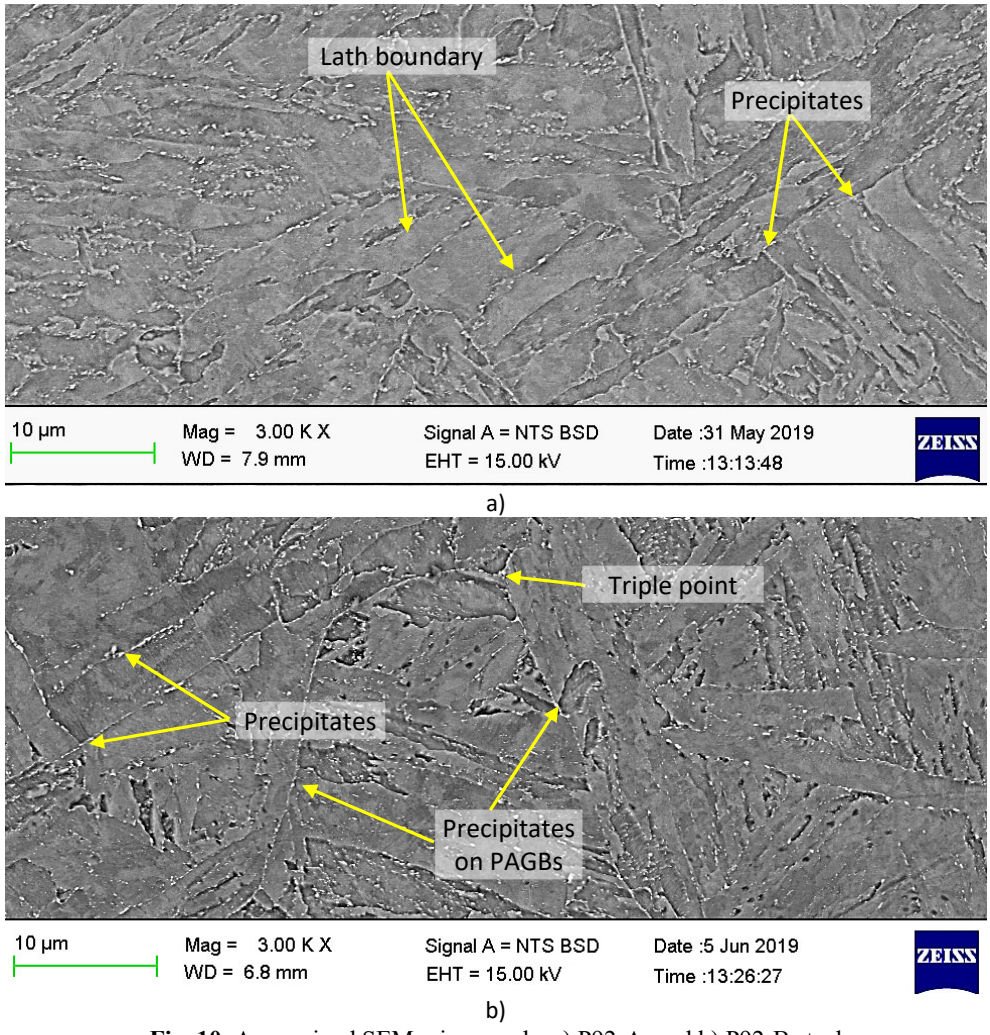

Fig. 10. As-received SEM micrographs a) P92-A, and b) P92-B steel

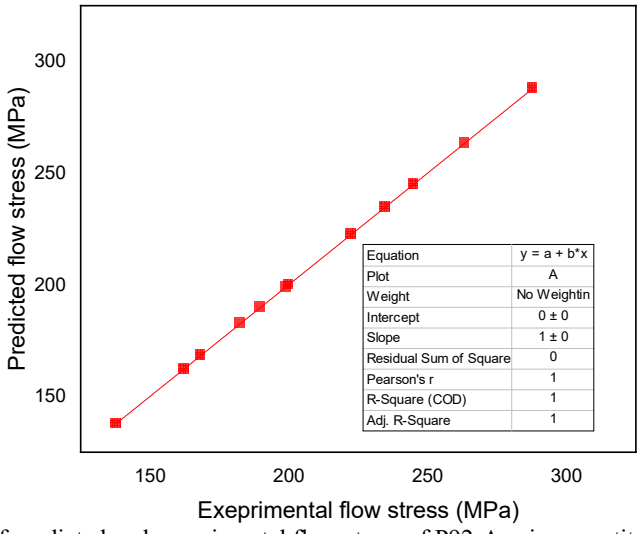

Fig. 11. Comparison of predicted and experimental flow stress of P92-A using constitutive equation of P92-B

From the flow stress results, it is not easy to say the effect of alloying elements on metal forming. A higher amount of alloying elements contributes to the formation of different phases that affect dislocation movement and grain boundary mobility (Nkhoma, 2014). The flow stress-strain curves show that P92-B had the highest stress values at all deformation conditions. Hence, it is logical that the calculated constitutive parameters (*n, A* and *Q*) will be different for the two steels. The differences can be due to the varied chemical composition of the two steels. For example, Yang *et al.* (2017) have shown that alloying elements affect activation energy. The addition of alloying elements results in high **Q** values for steel (Fedoseeva et al., 2016; McQueen & Ryan, 2002; Menapace et al., 2018), thus affecting the diffusivity of Fe in austenite and retardation of dynamic recrystallisation DRX (Carsí et al., 2011). Solute atoms such as Cr increase the number of precipitates resulting in solution strengthening. The presence of precipitates hinders dislocation motion, causing high activation energy (Ashby, 1972; Zhang et al., 2017).

Medina and Hernandez (1996) and Suikkanen *et al.* (2012) reported that boron (B) and carbon (C) reduce *Q* values by enhancing diffusion. Other alloying elements in steel have the opposite effect. Ferrite and austenite formers have either a negative or positive influence on the δ-ferrite formation, which affect the deformation process. The presence of δ-ferrite creates a large α-γ interfacial area for micro-void nucleation (Nkhoma, 2014). To this end, the higher Cr content contributed to solid solution strengthening, hence causing high flow stress, resulting in the differences in constitutive parameters reported in this study for the two steels. High-stress exponent values also increase the activation energy. The stress exponent **n** is affected significantly by flow stress. When the flow stress increases, the activation energy increases. The differences in higher **n** values for the two steels may be due to the interaction between the precipitates, thus hindering the forming of the material (Ennis et al., 1997). During deformation, different phases coexist in equilibrium at different deformation temperatures. These phases hinder dislocation resulting in higher stress exponent, as stress exponent values depend on the deformation temperature. The stress exponent also depends on the material chemistry and deformation conditions, thus affecting the flow stress. The effect of deformation conditions behaviour was seen in the log-log plots of strain rate versus hyperbolic sine (sinh (ασ)) flow stress, that the lines were not parallel to each other (Fig. 6a and Fig. 8a).

Structure factor **A** was: 2.44×10^{15} (P92-A) and 6.90×10^{19} (P92-B). The structure factor **A**-value depends on activation energy **Q,** which is affected by the deformation parameters and chemical composition (Shi & Liu, 2011). In this study, a high **Q**-value indicates a high **A**-value, and studies suggest the structure factor is proportional to activation energy (Nkhoma, 2014). The study reports that structure factor **A** depends on the activation energy, stress exponent and strain rate, as shown in **Fig. 6a** and **Fig. 8a**). The current study findings are also available in the literature.

3.4 Statistical error analysis

Fig. 12 shows the comparison of experimental and predicted data for the two steels investigated. The model was verified using statistical tools: average absolute relative error (*AARE*) and correlation coefficient (*R*). These tools verified the accuracy of the developed equation. The results show that the correlation coefficients (*R*) were: 0.995 (P92-A) and 0.995 (P92-B). These values were close to 1.0, which indicates a perfect correlation. However, this relationship only gives an approximation of the data. A good correlation between variables cannot depend on the correlation coefficient, as this parameter does not show effect or cause. Thus the predicting model may be biased towards the extremes values giving a higher correlation coefficient *R* (Wang et al., 2017). Therefore, statistical *AARE* analysis was used. This parameter determines the relative error step by step, thus giving the accuracy of the parameters measured. The smaller the AARE values, the higher the accuracy of

the variable (constitutive equation) predicting flow stress (Srinivasulu & Jain, 2006). The percentage error was P92-A: 1.84% and P92-B: 1.70%. The low *AARE* values show a higher accuracy of the constitutive model in predicting the flow stress (Li et al., 2018). The results analysed showed that the developed model has high accuracy in describing flow stress behaviour for the two steels tested.

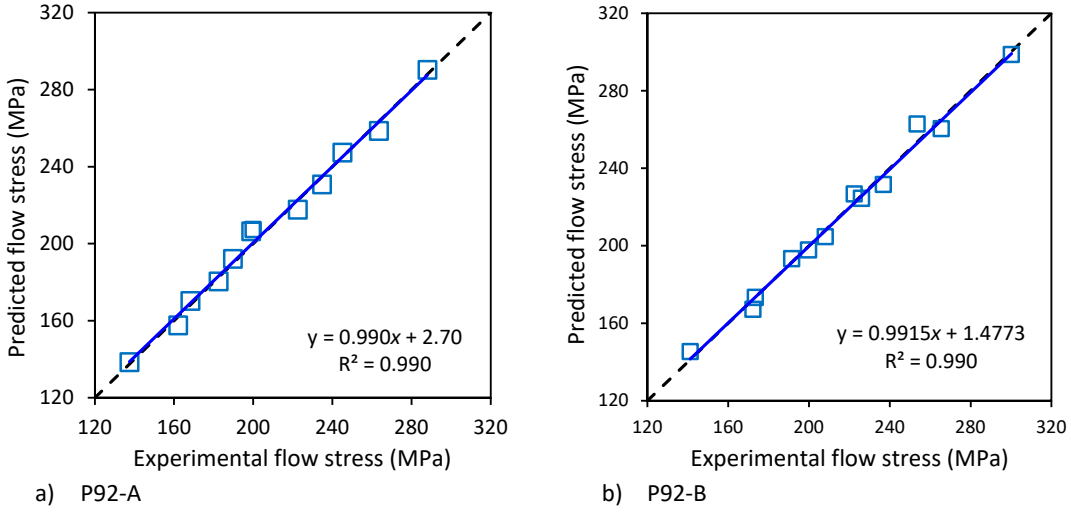

Fig. 12. Plot the experimental *vs.* predicted stress data

4. Conclusion

The hot deformation behaviour of two ASTM A335 P92 steel was studied in the thermal-mechanical equipment. Test conditions were: temperature (850-1000°C) and strain rate of 0.1-10s^{-1} for a strain of 0.5. Arrhenius constitutive equation constants were obtained by substituting the flow stress data and developing constitutive equations.

In conclusion:

1. The flow curves showed that work-hardening and dynamic softening (DRV) controlled the deformation process. The flow stress increased with a decrease in temperature and vice versa.
2. The hot deformation parameters were: stress exponent P92-A (9.0) and P92-B (11), and activation energy: P92-A (369 kJmol^{-1}) and P92-B (472 kJmol^{-1}). A hyperbolic-sine Arrhenius type constitutive equation developed for two P92 steel were as follows:

$$\textbf{P92-A:} \quad \dot{\varepsilon} = 2.44 \times 10^{15} \sinh(0.0049\sigma_{sat})^{9} \exp\left[\frac{-369000}{RT}\right]$$

$$\textbf{P92-B:} \quad \dot{\varepsilon} = 6.90 \times 10^{19} \sinh(0.0045\sigma_{sat})^{11} \exp\left[\frac{-471860}{RT}\right]$$

3. The metal forming can be can be analysed by the Zener-Hollomon parameter **Z.** For the two steels, the relationship between **Z**-parameter and flow stress had a linear correlation coefficient of 99%. The flow stress for the two steels can be determined by:

$$\textbf{P92-A:} \quad \sigma_{sat} = \frac{1}{0.0049} \ln\left[\left(\frac{Z}{2.44\times10^{15}}\right)^{\frac{1}{9}} + \left(\left(\frac{Z}{2.44\times10^{15}}\right)^{\frac{2}{9}} + 1\right)^{\frac{1}{2}}\right]$$

$$Z = \dot{\varepsilon}\left[\frac{369000}{RT}\right] = 2.44 \times 10^{15}(\sinh(0.0049\sigma_{sat})^{9}$$

$$\textbf{P92-B:} \quad \sigma_{sat} = \frac{1}{0.0045} \ln\left[\left(\frac{Z}{6.90\times10^{19}}\right)^{\frac{1}{11}} + \left(\left(\frac{Z}{6.90\times10^{19}}\right)^{\frac{2}{11}} + 1\right)^{\frac{1}{2}}\right]$$

$$Z = \dot{\varepsilon}\left[\frac{472000}{RT}\right] = 6.90 \times 10^{19} (\sinh(0.0045\sigma_{sat})^{11}$$

4. The differences in the material constants: *Q, n* and structure factor A may have been due to the differences in the chemical composition of the two steels. Study findings show that Cr content had a marginal effect on the flow stress behaviour. Apart from Cr, other alloying elements might have also caused the differences in material constants.
5. The constitutive model was verified using *R* and *AARE* parameters. These parameters showed a good relationship between the predicted and the experimental data. The study found out that either of the equations developed can accurately predict the flow stress behaviour of the other steel. Therefore, the derived equation is applicable in predicting the flow stress behaviour of P92 steel of similar or close chemical composition.

Acknowledgement

The authors thank the DSI-CSIR for financial support of this study.

References

Alsagabi, S. (2016). High Temperature Deformation Behavior of P92 Steel. *Transactions of the Indian Institute of Metals*, *69*(8), 1513–1518. https://doi.org/10.1007/s12666-015-0725-3

Ashby, M. F. (1972). A first report on deformation-mechanism maps. *Acta Metallurgica*, *20*(7), 887–897. https://doi.org/10.1016/0001-6160(72)90082-X

Cabrera, J. M., Al Omar, A., Jonas, J. J., & Prado, J. M. (1997). Modeling the flow behavior of a medium carbon microalloyed steel under hot working conditions. *Metallurgical and Materials Transactions A: Physical Metallurgy and Materials Science*, *28*(11), 2233–2243. https://doi.org/10.1007/s11661-997-0181-8

Carsí, M., Peñalba, F., Rieiro, I., & Ruano, O. A. (2011). High temperature workability behavior of a modified P92 steel. *International Journal of Materials Research*, *102*(11), 1378–1383. https://doi.org/10.3139/146.110603

Czyrska-filemonowicz, A., Zielińska-lipiec, A., & Ennis, P. J. (2006). Modified 9 % Cr Steels for Advanced Power Generation : Microstructure and Properties. *Journal of Achievements in Materials and Manufacturing Engineering*, *19*(2), 43–48.

David, S. A., Siefert, J. A., & Feng, Z. (2013). Welding and weldability of candidate ferritic alloys for future advanced ultrasupercritical fossil power plants. In *Science and Technology of Welding and Joining* (Vol. 18, Issue 8, pp. 631–651). https://doi.org/10.1179/1362171813Y.0000000152

El Wahabi, M., Cabrera, J. M., & Prado, J. M. (2003). Hot working of two AISI 304 steels: A comparative study. *Materials Science and Engineering A*, *343*(1–2), 116–125. https://doi.org/10.1016/S0921-5093(02)00357-X

Ennis, P. J., & Czyrska-Filemonowicz, A. (2003). Recent advances in creep-resistant steels for power plant applications. *Sadhana*, *28*(3–4), 709–730. https://doi.org/10.1007/BF02706455

Ennis, P. J., Zielinska-Lipiec, A., Wachter, O., & Czyrska-Filemonowicz, A. (1997). Microstructural stability and creep rupture strength of the martensitic steel P92 for advanced power plant. *Acta Materialia*, *45*(12), 4901–4907. https://doi.org/10.1016/S1359-6454(97)00176-6

Evans, R. W., & Scharning, P. J. (2001). Axisymmetric compression test and hot working properties of alloys. *Materials Science and Technology*, *17*(8), 995–1004. https://doi.org/10.1179/026708301101510843

Fedoseeva, A., Dudova, N., & Kaibyshev, R. (2016). Creep strength breakdown and microstructure evolution in a 3%Co modified P92 steel. *Materials Science and Engineering A*, *654*, 1–12. https://doi.org/10.1016/j.msea.2015.12.027

Francis, J. A., Mazur, W., & Bhadeshia, H. K. D. H. (2006). Review Type IV cracking in ferritic power plant steels. *Materials Science and Technology*, *22*(12), 1387–1395. https://doi.org/10.1179/174328406X148778

Funakawa, Y., & Ujiro, T. (2010). Tensile properties of chromium-bearing extra low carbon steel sheets. *ISIJ International*, *50*(10), 1488–1495. https://doi.org/10.2355/isijinternational.50.1488

He, A., Xie, G., Yang, X., Wang, X., & Zhang, H. (2015). A physically-based constitutive model for a nitrogen alloyed ultralow carbon stainless steel. *Computational Materials Science*, *98*, 64–69. https://doi.org/10.1016/j.commatsci.2014.10.044

He, A., Xie, G., Zhang, H., & Wang, X. (2013). A comparative study on Johnson-Cook, modified Johnson-Cook and Arrhenius-type constitutive models to predict the high temperature flow stress in 20CrMo alloy steel. *Materials and Design*, *52*, 677–685. https://doi.org/10.1016/j.matdes.2013.06.010

Huang, Y., Wang, S., Xiao, Z., & Liu, H. (2017). Critical Condition of Dynamic Recrystallization in 35CrMo Steel. *Metals*, *7*(5), 161. https://doi.org/10.3390/met7050161

Jha, J. S., Tewari, A., Mishra, S., & Toppo, S. (2017). Constitutive Relations for Ti-6Al-4V Hot Working. *Procedia Engineering*, *173*, 755–762. https://doi.org/10.1016/j.proeng.2016.12.089

Kishor, B., Chaudhari, G. P., & Nath, S. K. (2016). Hot Deformation Characteristics of 13Cr-4Ni Stainless Steel Using Constitutive Equation and Processing Map. *Journal of Materials Engineering and Performance*, *25*(7), 2651–2660. https://doi.org/10.1007/s11665-016-2159-4

Kumar, N., Kumar, S., Rajput, S. K., & Nath, S. K. (2017). Modelling of flow stress and prediction of workability by processing map for hot compression of 43CrNi steel. *ISIJ International*, *57*(3), 497–505. https://doi.org/10.2355/isijinternational.ISIJINT-2016-306

Laasraoui, A., & Jonas, J. J. (1991). Prediction of steel flow stresses at high temperatures and strain rates. *Metallurgical Transactions A*, *22*(7), 1545–1558. https://doi.org/10.1007/BF02667368

Li, N., Zhao, C., Jiang, Z., & Zhang, H. (2019). Flow behavior and processing maps of high-strength low-alloy steel during hot compression. *Materials Characterization*, *153*(October 2018), 224–233. https://doi.org/10.1016/j.matchar.2019.05.009

Li, Y., Ji, H., Li, W., Li, Y., Pei, W., & Liu, J. (2018). Hot deformation characteristics-Constitutive equation and processing maps-of 21-4N Heat- resistant steel. *Materials*, *12*(1). https://doi.org/10.3390/ma12010089

Lin, Y. C., Chen, M. S., & Zhang, J. (2009). Modeling of flow stress of 42CrMo steel under hot compression. *Materials Science and Engineering A*, *499*(1–2), 88–92. https://doi.org/10.1016/j.msea.2007.11.119

Lin, Y. C., Chen, M. S., & Zhong, J. (2008). Prediction of 42CrMo steel flow stress at high temperature and strain rate.

Mechanics Research Communications, *35*(3), 142–150. https://doi.org/10.1016/j.mechrescom.2007.10.002
Lin, Y. C., Li, L. T., Xia, Y. C., & Jiang, Y. Q. (2013). Hot deformation and processing map of a typical Al-Zn-Mg-Cu alloy. *Journal of Alloys and Compounds*, *550*, 438–445. https://doi.org/10.1016/j.jallcom.2012.10.114
Lin, Y. C., Xia, Y. C., Chen, X. M., & Chen, M. S. (2010). Constitutive descriptions for hot compressed 2124-T851 aluminum alloy over a wide range of temperature and strain rate. *Computational Materials Science*, *50*(1), 227–233. https://doi.org/10.1016/j.commatsci.2010.08.003
Liu, C. Y., Zhang, R. J., & Yan, Y. N. (2011). Hot deformation behaviour and constitutive modelling of P92 heat resistant steel. *Materials Science and Technology*, *27*(8), 1281–1286. https://doi.org/10.1179/026708310X12683158443323
Liu, X. G., Ji, H. P., Guo, H., Jin, M., Guo, B. F., & Gao, L. (2013). Study on hot deformation behaviour of 316LN austenitic stainless steel based on hot processing map. *Materials Science and Technology*, *29*(1), 24–29. https://doi.org/10.1179/1743284712Y.0000000083
Luan, J., Sun, C., Li, X., & Zhang, Q. (2014). Constitutive model for AZ31 magnesium alloy based on isothermal compression test. *Materials Science and Technology*, *30*(2), 211–219. https://doi.org/10.1179/1743284713Y.0000000341
Masuyama, F. (2001). History of power plants and progress in heat resistant steels. In *ISIJ International* (Vol. 41, Issue 6, pp. 612–625). https://doi.org/10.2355/isijinternational.41.612
McQueen, H. J., & Ryan, N. D. (2002). Constitutive analysis in hot working. *Materials Science and Engineering A*, *322*(1–2), 43–63. https://doi.org/10.1016/S0921-5093(01)01117-0
Medina, S. F., & Hernandez, C. A. (1996). General expression of the Zener-Hollomon parameter as a function of the chemical composition of low alloy and microalloyed steels. *Acta Materialia*, *44*(1), 137–148. https://doi.org/10.1016/1359-6454(95)00151-0
Mehtonen, S. V., Karjalainen, L. P., & Porter, D. a. (2014). Modeling of the high temperature flow behavior of stabilized 12–27wt% Cr ferritic stainless steels. *Materials Science and Engineering: A*, *607*, 44–52. https://doi.org/10.1016/j.msea.2014.03.124
Menapace, C., Sartori, N., Pellizzari, M., & Straffelini, G. (2018). Hot Deformation Behavior of Four Steels: A Comparative Study. *Journal of Engineering Materials and Technology, Transactions of the ASME*, *140*(2), 021006. https://doi.org/10.1115/1.4038670
Milović, L., Vuherer, T., Blačić, I., Vrhovac, M., & Stanković, M. (2013). Microstructures and mechanical properties of creep resistant steel for application at elevated temperatures. *Materials and Design*, *46*, 660–667. https://doi.org/10.1016/j.matdes.2012.10.057
Mirzadeh, H. (2015). Constitutive modeling and prediction of hot deformation flow stress under dynamic recrystallization conditions. *Mechanics of Materials*, *85*, 66–79. https://doi.org/10.1016/j.mechmat.2015.02.014
Mirzadeh, H., Cabrera, J. M., Prado, J. M., & Najafizadeh, A. (2011). Hot deformation behavior of a medium carbon microalloyed steel. *Materials Science and Engineering A*, *528*(10–11), 3876–3882. https://doi.org/10.1016/j.msea.2011.01.098
Mostafaei, M. A., & Kazeminezhad, M. (2012). The prediction of hot flow behavior of Al-6%Mg alloy. *Materials Science and Engineering A*, *535*, 216–221. https://doi.org/10.1016/j.msea.2011.12.067
Nkhoma, R. C. K. (2014). Hot workability of AISI 321 and AISI 304 austenitic stainless steels. *Journal of Alloys and Compounds*, *595*, 103–112. https://doi.org/10.1016/j.jallcom.2014.01.157
Obiko, J., Chown, L. H., & Whitefield, D. J. (2019). Warm deformation behaviour of P92 steel. *Materials Research Express*, *6*(12). https://doi.org/10.1088/2053-1591/ab5e9c
Ohgami, M., Naoi, H., Kinbara, S., Mimura, H., Ikemoto, T., & Fujita, T. (1997). Development of 9CrW tube, pipe and forging for ultra supercritical power plant boilers. In *Nippon Steel Technical Report* (Issue 72, pp. 59–64).
Oudin, A., Barnett, M. R., & Hodgson, P. D. (2004). Grain size effect on the warm deformation behaviour of a Ti-IF steel. *Materials Science and Engineering A*, *367*(1–2), 282–294. https://doi.org/10.1016/j.msea.2003.10.273
Qian, L. Y., Fang, G., Zeng, P., & Wang, L. X. (2015). Correction of flow stress and determination of constitutive constants for hot working of API X100 pipeline steel. *International Journal of Pressure Vessels and Piping*, *132–133*(November), 43–51. https://doi.org/10.1016/j.ijpvp.2015.05.008
Rastegari, H., Kermanpur, A., Najafizadeh, A., Porter, D., & Somani, M. (2015). Warm deformation processing maps for the plain eutectoid steels. *Journal of Alloys and Compounds*, *626*, 136–144. https://doi.org/10.1016/j.jallcom.2014.11.170
Sakthivel, T., Selvi, S. P., & Laha, K. (2015). An assessment of creep deformation and rupture behaviour of 9Cr-1.8W-0.5Mo-VNb (ASME grade 92) steel. *Materials Science and Engineering A*, *640*, 61–71. https://doi.org/10.1016/j.msea.2015.05.068
Sakthivel, T., Selvi, S. P., Parameswaran, P., & Laha, K. (2016). Creep deformation and rupture behaviour of thermal aged P92 steel. *Materials at High Temperatures*, *33*(1), 33–43. https://doi.org/10.1179/1878641315Y.0000000016
Samantaray, D., Mandal, S., & Bhaduri, A. K. (2010). Constitutive analysis to predict high-temperature flow stress in modified 9Cr-1Mo (P91) steel. *Materials and Design*, *31*(2), 981–984. https://doi.org/10.1016/j.matdes.2009.08.012
Samantaray, D., Phaniraj, C., Mandal, S., & Bhaduri, A. K. (2011). Strain dependent rate equation to predict elevated temperature flow behavior of modified 9Cr-1Mo (P91) steel. *Materials Science and Engineering A*, *528*(3), 1071–1077. https://doi.org/10.1016/j.msea.2010.10.036
Samuel, E. I., Choud, B. K., Palaparti, D. P. R., & Mathew, M. D. (2013). *Creep Deformation and Rup pture Behaviour of P92 Steel at 92 23 K*. *55*, 64–69. https://doi.org/10.1016/j.proeng.2013.03.220
Sellars, C. M., & McTegart, W. J. (1966). On the mechanism of hot deformation. *Acta Metallurgica*, *14*(9), 1136–1138.

https://doi.org/10.1016/0001-6160(66)90207-0
Shi, R. X., & Liu, Z. D. (2011). Hot deformation behavior of P92 steel used for ultra-super-critical power plants. *Journal of Iron and Steel Research International*, *18*(7), 53–58. https://doi.org/10.1016/S1006-706X(11)60090-3
Srinivasulu, S., & Jain, A. (2006). A comparative analysis of training methods for artificial neural network rainfall-runoff models. *Applied Soft Computing Journal*, *6*(3), 295–306. https://doi.org/10.1016/j.asoc.2005.02.002
Suikkanen, P. P., Lang, V. T. E., Somani, M. C., Porter, D. A., & Karjalainen, L. P. (2012). Effect of Silicon and Aluminium on Austenite Static Recrystallization Kinetics in High-strength TRIP-aided Steels. *ISIJ International*, *52*(3), 471–476. https://doi.org/10.2355/isijinternational.52.471
Sun, S. L., Zhang, M. G., & He, W. W. (2010). Hot deformation behavior and hot processing map of P92 steel. *Advanced Materials Research*, *97–101*, 290–295. https://doi.org/10.4028/www.scientific.net/AMR.97-101.290
Tabuchi, M., Watanabe, T., Kubo, K., Matsui, M., Kinugawa, J., & Abe, F. (2001). Creep crack growth behavior in the HAZ of weldments of W containing high Cr steel. *International Journal of Pressure Vessels and Piping*, *78*(11–12), 779–784. https://doi.org/10.1016/S0308-0161(01)00090-4
Výrostková, A., Homolová, V., Pecha, J., & Svoboda, M. (2008). Phase evolution in P92 and E911 weld metals during ageing. *Materials Science and Engineering A*, *480*(1–2), 289–298. https://doi.org/10.1016/j.msea.2007.07.036
Wan, Z., Hu, L., Sun, Y., Wang, T., & Li, Z. (2018). Hot deformation behavior and processing workability of a Ni-based alloy. *Journal of Alloys and Compounds*, *769*, 367–375. https://doi.org/10.1016/j.jallcom.2018.08.010
Wang, L., Liu, F., Zuo, Q., & Chen, C. F. (2013). Prediction of flow stress for N08028 alloy under hot working conditions. *Materials and Design*, *47*, 737–745. https://doi.org/10.1016/j.matdes.2012.12.074
Wang, M., Jin, P., & Wang, J. (2014). Hot deformation and processing maps of 7005 aluminum alloy. *High Temperature Materials and Processes*, *33*(4), 369–375. https://doi.org/10.1515/htmp-2013-0083
Wang, S., Huang, Y., Xiao, Z., Liu, Y., & Liu, H. (2017). A Modified Johnson-Cook Model for Hot Deformation Behavior of 35CrMo Steel. *Metals*, *7*(9), 337. https://doi.org/10.3390/met7090337
Yan, P., Liu, Z. dong, Liu, W., Bao, H. sheng, & Weng, Y. qing. (2013). Hot deformation behavior of a new 9%Cr heat resistant steel G115. *Journal of Iron and Steel Research International*, *20*(9), 73–79. https://doi.org/10.1016/S1006-706X(13)60159-4
Yang, Z. N., Dai, L. Q., Chu, C. H., Zhang, F. C., Wang, L. W., & Xiao, A. P. (2017). Effect of Aluminum Alloying on the Hot Deformation Behavior of Nano-bainite Bearing Steel. *Journal of Materials Engineering and Performance*, *26*(12), 5954–5962. https://doi.org/10.1007/s11665-017-3018-7
Yang, Z., Zhang, F., Zheng, C., Zhang, M., Lv, B., & Qu, L. (2015). Study on hot deformation behaviour and processing maps of low carbon bainitic steel. *Materials and Design*, *66*(PA), 258–266. https://doi.org/10.1016/j.matdes.2014.10.068
Yanushkevich, Z., Lugovskaya, A., Belyakov, A., & Kaibyshev, R. (2016). Deformation microstructures and tensile properties of an austenitic stainless steel subjected to multiple warm rolling. *Materials Science and Engineering A*, *667*, 279–285. https://doi.org/10.1016/j.msea.2016.05.008
Yatomi, M., Fuji, A., Tabuchi, M., Hasegawa, Y., Kobayashi, K. I., Yokobori, T., & Yokobori, T. (2010). Evaluation of Creep Crack Growth Rate of P92 Welds Using Fracture Mechanics Parameters. *Journal of Pressure Vessel Technology*, *132*(4), 041404. https://doi.org/10.1115/1.4001522
Zhang, P., Yi, C., Chen, G., Qin, H., & Wang, C. (2016). Constitutive Model Based on Dynamic Recrystallization Behavior during Thermal Deformation of a Nickel-Based Superalloy. *Metals*, *6*(7), 161. https://doi.org/10.3390/met6070161
Zhang, X. Z., Wu, X. J., Liu, R., Liu, J., & Yao, M. X. (2017). Deformation-mechanism-based modeling of creep behavior of modified 9Cr-1Mo steel. *Materials Science and Engineering A*, *689*(February), 345–352. https://doi.org/10.1016/j.msea.2017.02.044
Zhu, L., He, J., & Zhang, Y. (2018). A two-stage constitutive model of X12CrMoWVNbN10-1-1 steel during elevated temperature. *Materials Research Express*, *5*, 1–11.
Zhu, Y. yang, Ning, L. kui, Xin, T. zheng, Liu, E. ze, Tong, J., Tan, Z., Zhou, Y. tao, & Zheng, Z. (2021). Hot deformation behavior and microstructure evolution of an Fe–30Cr–2Mo ultra-pure super ferritic stainless steel. *Journal of Iron and Steel Research International*, *28*(10), 1291–1304. https://doi.org/10.1007/s42243-021-00584-4